International Journal of Advanced Robotic Systems

OPEN ACCESS ARTICLE

Metrological Evaluation of a Novel Medical Robot and Its Kinematic Calibration

Regular Paper

Longfei Zhao[1]*, Ahmed Joubair[1], Pascal Bigras[1] and Ilian A. Bonev[1]

1 Ecole de technologie superieure, Montreal, Quebec, Canada
*Corresponding author(s) E-mail: longfei.zhao@yahoo.com

Received 23 December 2014; Accepted 16 May 2015

DOI: 10.5772/60881

Abstract

The vessels are twisted in a longitudinal 3D space in the lower limbs of humans. Thus, it is difficult to perform an ultrasound scanning examination in this area. In this paper, a new medical parallel robot is introduced to effectively diagnose vessel disease in the lower limbs. The robot's position repeatability and accuracy are evaluated. Furthermore, the robot's accuracy is improved through a calibration process in which the kinematic parameters are identified through a simple identification approach.

Keywords Medical Robot, Parallel Robot, Kinematic Calibration, Laser Tracker

1. Introduction

Ultrasound (US) scanning examination is one of the major diagnostic modalities in daily medicine. It shows advantages in low cost and non-radiation to the human body. However, a survey reveals that the repetitive strain of daily US examination over many hours causes musculoskeletal disorders to sonographers [1]. Thus, much research is engaged towards the design of medical robots to perform the US scanning examination. Furthermore, the US medical robot can collect position data during the examination process, which provides the essential information for 3D reconstruction of the scanned area.

Several works on US medical robots have been performed. A portable US medical robot was proposed in a tele-scanning robot project [2]. It has four degrees of freedom (DOF) and assists a doctor in controlling a US probe remotely. The robot prototype is extended to 6 DOF in the OTELO project [3]. It is agile and able to cover the large scan area. Nevertheless, the US scanning examination requires an assistant to hold the robot during the examination process. In general, the portable medical US robot does not reduce the workload of sonographers. Many US medical robot systems are developed based on industrial robots. The Hippocrate system employs a PA-10 robot arm from Mitsubishi Heavy Industry to scan the carotid artery [4]. An F3 industrial robot from CRS Robotics was used in [5] to diagnose breast cancer. A lightweight robot LWR from KUKA was used in [6] to assist the sonographer. However, the industrial robots are mostly designed for general use, and medical applications are limited due to the closed architecture of the controllers. Thus, some serial robots are designed for US medical implement, such as an abdominal US scanning robot in [7], and a self-balanced robot from the University of British Columbia [8, 9]. Serial robots, however, have relatively low stiffness and their position errors are accumulated and amplified from link to link. Besides, the motors are generally mounted on links successively. Thus, each link has to support the weight of all the subsequent links and actuators. Several medical US robots were designed with parallel structures. A parallel robot was developed to hold the US probe in [10]. It consists of three legs displaced on both sides of the patient and a probe gripper hanging over the scanned area. A cable robot was developed in the TER project [11]. A sliding mechanism was used in a parallel robot to perform echo-graphic diagnosis [12, 13]. The patient has to support the weight of the robot since the mechanism is placed on the scanning area. WTA-2R was designed to hold the US probe and perform an automated scanning based on US image feedback in [14].

The medical robots mentioned above are mainly designed for carotid or abdominal US scanning, and are not appropriate for examination in the lower limbs due to their limited workspace, dexterity, etc. MedRUE (for **Med**ical **R**obot for vascular **U**ltrasound **E**xamination) is a new parallel robot designed to perform US scanning examination in lower limbs, improved based on its first concept proposed in [15]. It has a longitudinal workspace aligned with the patient's leg, but relatively small size and low weight [16]. Since MedRUE needs to know the position of its end-effector with high accuracy, in order to reconstruct a 3D volume from US images it needs to be calibrated.

The calibration of a US medical robot involves probe calibration and kinematic calibration. The probe calibration identifies the constant transformation between the probe body and US image [17, 18]. However, in this article we focus only on the kinematic calibration of the robot. The kinematic calibration methods for serial robots are mostly on identifying the Denavit-Hartenberg parameters [19, 20]. These parameters are widely used to develop the kinematic model of serial robots. However, they are not always the simplest way to model parallel robots. The calibration methods of parallel robots vary depending on the different geometric structures of parallel robots. There are many calibration studies regarding planar robots, the Gough-Stewart platform and the Delta robot [21-25].

In this paper, we present a new medical robot with its repeatability and accuracy assessment. The position accuracy is improved by a calibration method based on direct position measurements with a laser tracker. The method is easy to implement on the robot without elaborate knowledge of the advanced kinematic calibration. In addition, the proposed calibration method identifies kinematic parameters individually, and the nonlinear interferences between kinematic parameters are significantly reduced. Therefore, the identified kinematic parameters are more accurate, and are important for further research, such as temporal stiffness calibration. By contrast, other calibration methods using optimization identify all kinematic parameters simultaneously [26-28]. The optimization approach may achieve better end-effector position accuracy, but it sacrifices precision for individual parameters. The MedRUE robot is briefly described in section 2 and its kinematic model and calibrated parameters are presented. Section 3 discusses the assessment of repeatability and accuracy. Then, the proposed calibration method and the result are demonstrated in section 4. At the end, a conclusion is addressed in section 5.

2. Robot description and kinematics

In this section, the new medical robot is introduced and its intuitive kinematic model is discussed. The kinematic model considers the errors of link lengths and offsets which need to be calibrated, and thereafter the calibrated parameters are listed. The robot base reference frame ($\mathbf{\Phi}_0$) and the world reference frame ($\mathbf{\Phi}_W$) are also defined in this section. The parameters to describe these two frames are identified with a laser tracker.

2.1 Introduction of MedRUE

MedRUE (Medical Robot for vascular Ultrasound Examination) is a prototype of medical parallel robot designed for the diagnosis of the peripheral arterial disease in the lower limbs.

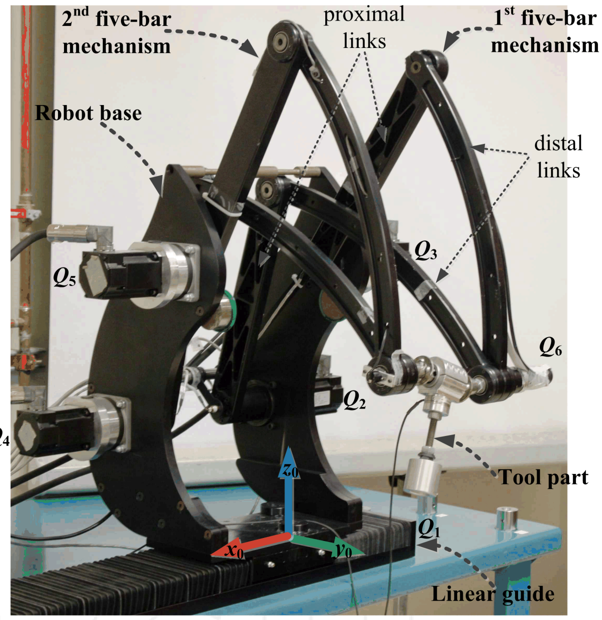

Figure 1. MedRUE: a new prototype of medical US robot

As shown in Figure 1, MedRUE is a 6-DOF parallel robot consisting of a robot base with a linear guide, two five-bar mechanisms and the *tool part* to carry the US probe. The U-shaped robot base is mounted on a linear guide (driven by actuator Q_1). The two five-bar mechanisms are assembled symmetrically on the robot's base, and are driven by actuators Q_2, Q_3, Q_4 and Q_5. Considering the first five-bar mechanism as an example, the two links driven by actuators are called *proximal links*, and the two links farther from the robot base are called *distal links*. The distal links connect at the shaft of the tool part. The tool part consists of a force/torque sensor and a dummy probe at the end. It is driven to rotate along the shaft by a small actuator Q_6 mounted on a distal link.

Since most actuators of MedRUE are located on the robot's base, the links of the five-bar mechanisms do not need to bear the heavy load of motors. Thus, the robot is relatively lightweight and agile. The linear guide extends the workspace along the length of the patient's leg and the curved distal links avoid mechanical interferences between the robot arms and the patient leg during the examination.

Frame $\mathbf{\Phi}_0$, also referred to as the robot frame, is defined on the robot base plate. The top surface of the robot base plate is defined as the x_0y_0 plane, and its normal is the z_0 axis. The linear guide determines the direction of the x_0 axis, and then the front side of the robot is the direction of y_0 axis. The origin of $\mathbf{\Phi}_0$ is located in the front centre hole of the bottom plate.

2.2 Kinematic model of MedRUE

The kinematic model of MedRUE and its kinematic parameters are illustrated in Figure 2. The two five-bar mechanisms are symmetrically assembled on the robot's base, and can therefore be modelled in the same way. As shown in Figure 2(a), the links of the i^{th} five-bar mechanism are named L_{ij}, where $i=1,2$ and $j=0,\dots,4$. The corresponding link lengths are denoted by l_{ij}. Link L_{i0} is fixed on the robot's base with an angle θ_i offset. Four actuators Q_{2i} and Q_{2i+1} are mounted on the robot's base, and the corresponding active joint variables are q_{2i} and q_{2i+1} at A_i and C_i respectively. The other joints q_{Bi}, q_{Di} and q_{DEi} are passive. The two five-bar mechanisms are parallel to the y_0z_0 plane. In Figure 2(b), the tool part connects the two five-bar mechanisms at E_i (with an offset d_{ei}). Two universal joints are located at F_i (with an offset d_{fi}) to provide orientation of the probe-support. The synchronized motion (i.e., same speed and direction) of two five-bar mechanisms provide translation motions to the tool part, while the unsynchronized motion provides rotation motions. During the rotational motion, the distance variation between the two universal joints F_i is compensated by a passive translation joint located between the probe-support and F_2. Actuator Q_6 is attached on L_{14} to provide a rotation motion of the tool part along x_0. The probe-support is considered as the wrist of MedRUE, and a reference frame $\mathbf{\Phi}_w$ is located at its geometric centre. Axis x_w is collinear with vector $\overrightarrow{F_1F_2}$ and z_w is pointing to the probe tip.

Given the joint values $(q_1,\dots, q_6)$, the forward kinematic solution of MedRUE can be obtained as follows:

Since A_i and C_i are static w.r.t. $\mathbf{\Phi}_0$, for the i^{th} $(i=1,2)$ five-bar mechanism, the coordinates of A_i and C_i are represented as:

$$\mathbf{a}_i = \begin{bmatrix} x_{O_i} & y_{O_i} - \frac{l_{i0}}{2}\sin\theta_i & z_{O_i} + \frac{l_{i0}}{2}\cos\theta_i \end{bmatrix}, \tag{1}$$

$$\mathbf{c}_i = \begin{bmatrix} x_{O_i} & y_{O_i} + \frac{l_{i0}}{2}\sin\theta_i & z_{O_i} - \frac{l_{i0}}{2}\cos\theta_i \end{bmatrix}^T \tag{2}$$

where O_i is the midpoint of L_{i0} with

$$x_{O_i} = d_{ei} + q_1 + \tilde{q}_1, \tag{3}$$

and $\tilde{q}_k$ is the offset error of k^{th} active joint. Then the coordinates of B_i and D_i are

$$\mathbf{b}_i = \mathbf{a}_i + l_{i1}\Psi\left(q_{2i} + \tilde{q}_{2i}\right), \tag{4}$$

$$\mathbf{d}_i = \mathbf{c}_i + l_{i3}\Psi\left(q_{2i+1} + \tilde{q}_{2i+1}\right), \tag{5}$$

where $\Psi(\varphi)=[0 \quad -\sin(\varphi) \quad \cos(\varphi)]^T$.

With the coordinates of B_i and D_i, all side lengths of the triangle $B_iD_iE_i$ are known. Then, the coordinates of E_i are obtained as

$$\mathbf{e}_i = \mathbf{d}_i + \overrightarrow{D_iH_i} + \overrightarrow{H_iE_i}, \tag{6}$$

where

$$\overrightarrow{D_iH_i} = \frac{l_{i4}^2 - l_{i2}^2 + \left\|\overrightarrow{D_iB_i}\right\|^2}{2\left\|\overrightarrow{D_iB_i}\right\|}\mathbf{u}_{\overrightarrow{D_iB_i}}, \tag{7}$$

$$\overrightarrow{H_iE_i} = \sqrt{l_{i4}^2 - \left\|\overrightarrow{D_iH_i}\right\|^2}\begin{bmatrix} 0 & -1 & 0 \\ 1 & 0 & 0 \\ 0 & 0 & 0 \end{bmatrix}\mathbf{u}_{\overrightarrow{D_iB_i}}, \tag{8}$$

and $\mathbf{u}$ represents a unit vector. As shown in Figure 2(a), F_i has an offset d_{fi}–d_{ei} w.r.t. E_i along x_0. Thus, the coordinates of F_i are

$$\mathbf{f}_i = \mathbf{D}(d_{fi} - d_{ei}, 0, 0)\mathbf{e}_i \tag{9}$$

where $\mathbf{D}(x,y,z)$ is the translation operation.

Assuming the orientation of the wrist reference frame $\mathbf{\Phi}_w$ is represented in the XYZ Euler angles, then

$$\mathbf{R}\left(\gamma,\beta,\alpha\right)\begin{bmatrix} 1 \\ 0 \\ 0 \end{bmatrix} = \mathbf{u}_{\overrightarrow{F_1F_2}} = \begin{bmatrix} u_x \\ u_y \\ u_z \end{bmatrix} \tag{10}$$

where $\mathbf{R}(\gamma, \beta, \alpha)$ is the rotation matrix. Since actuator Q_6 is fixed on L_{14}, the first Euler angle is obtained as

$$\gamma = q_{DE_1} + q_6 + \tilde{q}_6 \tag{11}$$

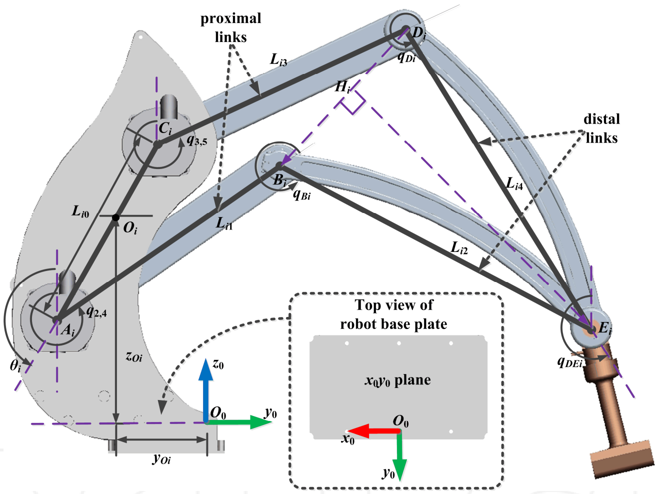

(a)

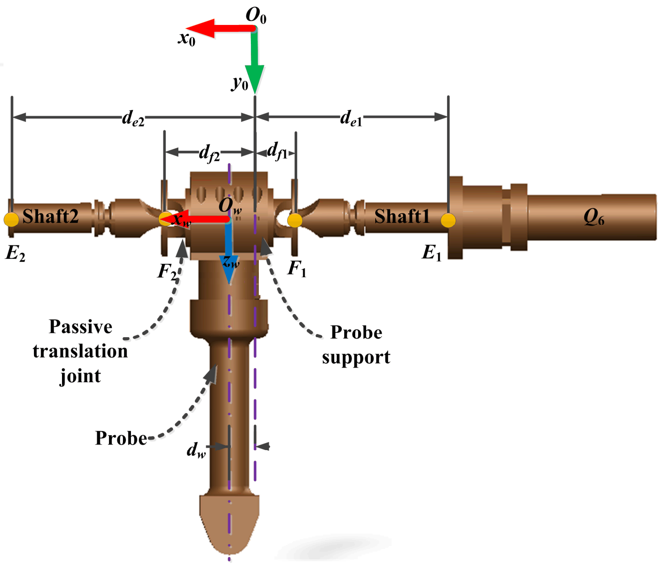

(b)

Figure 2. Kinematic model and parameters of MedRUE: (a) five-bar mechanism and robot base; (b) the tool part

where q_{DE_1}=atan2$\left(-\left(y_{E_1}-y_{D_1}\right), z_{E_1}-z_{D_1}\right)$. The other two Euler angles are obtained by substituting Eq. (11) into Eq. (10):

$$\alpha=\sin^{-1}\left(u_y\cos\gamma+u_z\sin\gamma\right), \tag{12}$$

$$\beta=\sin^{-1}\left(\frac{u_y\sin\gamma-u_z\cos\gamma}{\cos\alpha}\right). \tag{13}$$

Thus, the coordinates of O_w w.r.t. $\mathbf{\Phi}_0$ are

$$\mathbf{p}_w=\mathbf{f}_1+\mathbf{R}\left(\gamma,\beta,\alpha\right)\left[d_{f1}+d_w \quad 0 \quad 0\right]^T. \tag{14}$$

In our calibration process, a spherically mounted retroreflector (SMR) is attached to the probe. The coordinates of the SMR centre w.r.t. $\mathbf{\Phi}_w$ are x_S, y_S and z_S. Thus the coordinates of SMR w.r.t. $\mathbf{\Phi}_0$ are

$$\mathbf{p}_S=\mathbf{p}_w+\mathbf{R}\left(\gamma,\beta,\alpha\right)\left[x_S \quad y_S \quad z_S\right]^T. \tag{15}$$

Assuming the transformation matrix from the world reference frame $\mathbf{\Phi}_W$ to $\mathbf{\Phi}_0$ is represented by six parameters x_W, y_W, z_W, γ_W, β_W and α_W. Then $\mathbf{p}_S$ is represented w.r.t. $\mathbf{\Phi}_W$ as:

$${}^W\mathbf{p}_S={}^0_W\mathbf{T}^{-1}\mathbf{p}_S \tag{16}$$

where ${}^0_W\mathbf{T}=\mathbf{D}(x_W, y_W, z_W)\mathbf{R}(\gamma_W, \beta_W, \alpha_W)$.

3. Repeatability and Accuracy Assessment

In this section, robot repeatability and accuracy are assessed before calibration. Our assessment method is an adaptation of the international standard on robot performance and test method (ISO-9283) [29]. The nominal kinematic model (i.e., the model before calibration) is assessed in this section, and the calibrated kinematic model is validated in section 4.

In the nominal kinematic model [16], the corresponding parameters of the two five-bar mechanisms in Figure 2 are identical (*e.g.*, $l_{1j} = l_{2j}$, $j = 0,..., 4$). Moreover, each five-bar mechanism is symmetrically designed. In other words, the proximal links are identical ($l_{i1} = l_{i3}$, $i = 1, 2$), and so are the distal links ($l_{i2} = l_{i4}$, $i = 1, 2$). The offset joint values are considered to be equal to zero.

3.1 Robot path design and measurement points

In our implementation, the position accuracy has the priority since it is required both for safety reasons and 3D reconstruction. Orientation errors can be compensated in the 3D reconstruction with well-developed techniques, such as scale-invariant feature transform. In this article, only the position repeatability and accuracy are studied, while the orientation is kept constant during the measurement procedure. Before taking measurements, it is necessary to define the robot trajectory and the measured positions during data acquisition.

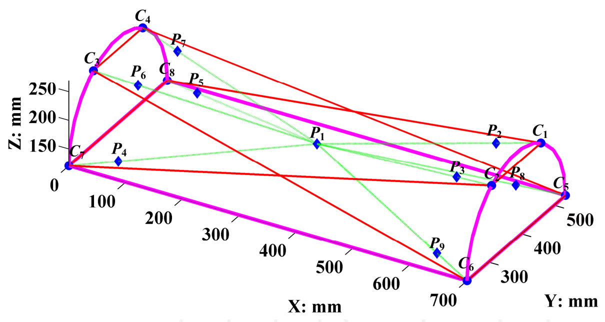

(a)

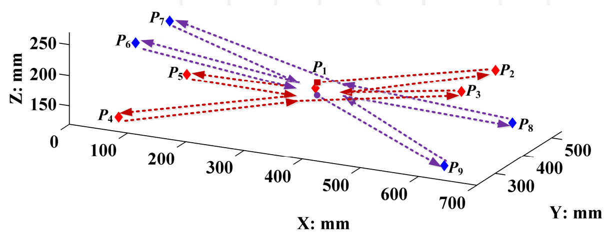

(b)

Figure 3. The measurement points in the workspace of MedRUE: (a) measurement points definition, (b) measurement path

Knowing that the robot is dedicated to lower limb scans, the effective robot's workspace is considered to be a half-cylinder, which covers the top surface area of a patient's leg. As shown in Figure 3(a), nine measurement points P_i (i = 1,..., 9) are considered in this target workspace. Namely, eight corners C_j (j = 1,..., 8) are created on both sides of the target workspace and form two planes $C_1C_2C_7C_8$ as well as $C_3C_4C_5C_6$. Point P_1 is located at the barycentre of all eight corners. Point P_2 is defined on the vector $\overrightarrow{P_1C_1}$, with $\| \overrightarrow{P_1P_2} \| = 0.8 \| \overrightarrow{P_1C_1} \|$, points P_3 to P_9 are similarly defined.

The used measurement path is an extension of the path design proposed in [30]. The robot end-effector is initially located at P_1, and trajectory of the robot end-effector is demonstrated in Figure 3(b). When the process started, the robot end-effector followed the trajectory on the plane $C_3C_4C_5C_6$, which is composed of the sequence $P_9 \to P_1 \to P_8 \to P_1 \to P_7 \to P_1 \to P_6 \to P_1$. Then, the robot trajectory continues on the plane $C_1C_2C_7C_8$, and follows the sequence $P_5 \to P_1 \to P_4 \to P_1 \to P_3 \to P_1 \to P_2 \to P_1$ to finish a measurement cycle. In our experiment, 30 measurement cycles are taken.

In this method, P_1 is visited from eight different directions, while all other measurement points are visited in a unidirectional approach (direction from P_1). Thus, the experiment design is used to estimate multidirectional repeatability at position P_1 and unidirectional repeatability at positions P_2 to P_8.

3.2 Accuracy and repeatability definition

At each measurement point P_i (i = 1,..., 9), the position of the end-effector is measured n times, where n = 8 directions × 30 cycles = 240 at P_1, and n = 30 at each of the other eight measurement points. A set of n measurements on a measurement point P_i is called a *cluster* of P_i. For any cluster, the *barycentre* is defined as a virtual point whose coordinates $[\bar{x}_i \;\; \bar{y}_i \;\; \bar{z}_i]$ are the mean values of all the n measurements:

$$\bar{x}_i = \frac{1}{n}\sum_{\eta=1}^{n} x_{i\eta}, \tag{17}$$

$$\bar{y}_i = \frac{1}{n}\sum_{\eta=1}^{n} y_{i\eta}, \tag{18}$$

$$\bar{z}_i = \frac{1}{n}\sum_{\eta=1}^{n} z_{i\eta}, \tag{19}$$

The distance between the η^{th} cycle measurement at P_i and the barycentre of the cluster of P_i is

$$l_{i\eta} = \sqrt{\left(x_{i\eta} - \bar{x}_i\right)^2 + \left(y_{i\eta} - \bar{y}_i\right)^2 + \left(z_{i\eta} - \bar{z}_i\right)^2}. \tag{20}$$

Then the repeatability at P_i is defined as follows:

$$RP_{P_i} = \bar{l}_i + 3S_{li}, \tag{21}$$

where $\bar{l}_i = \frac{1}{n}\sum_{\eta=1}^{n} l_{i\eta}$ and $S_{li} = \sqrt{\frac{\sum_{\eta=1}^{n}\left(l_{i\eta} - \bar{l}_i\right)^2}{n-1}}$.

The absolute position accuracy of P_i is defined by

$$APA_i = \sqrt{\left(\bar{x}_i - \hat{x}_i\right)^2 + \left(\bar{y}_i - \hat{y}_i\right)^2 + \left(\bar{z}_i - \hat{z}_i\right)^2}, \quad (22)$$

where $\hat{x}_i$, $\hat{y}_i$ and $\hat{z}_i$ are the command positions (reference positions) of P_i, and $\bar{x}$, $\bar{y}$ and $\bar{z}$ are barycentre coordinates defined in Eqs. (17) to (19).

MeRUE will be used to take US images at prescribed intervals. These US images will then be used to reconstruct the 3D model of the blood vessel. For the purposes of medical examination, the accuracy in measuring the position of a given US image is important w.r.t. the neighbouring images. In other words, the relative accuracy is important for our robot.

A *relative position accuracy* of a point can be defined as the accuracy of the distance between adjacent points (e.g., the distance accuracy between P_1 and P_2). Since each point P_i (i = 2,..., 9) is reached starting from P_1 in Figure 3(b), the nominal relative displacement of P_i (i = 2,..., 9) is calculated as follows:

$$\hat{\boldsymbol{\delta}}_i = \hat{\mathbf{p}}_i - \hat{\mathbf{p}}_1,\ i = 2,\ldots,9 \quad (23)$$

where $\hat{\mathbf{p}}_i$ is the nominal coordinates vector. Then Eq. (22) is modified to compute the relative position accuracy as

$$RPA_i = \left\|\boldsymbol{\delta}_i - \hat{\boldsymbol{\delta}}_i\right\|, i = 2,\ldots,9 \quad (24)$$

where $\boldsymbol{\delta}_i = \mathbf{p}_i - \mathbf{p}_{1i}$ is the measured relative displacement based on laser tracker. The notation $\mathbf{p}_{1i}$ is the measurement value of P_1 before moving towards to each P_i (i = 2,..., 9).

3.3 Experiment setup and results

The measurement setup is shown in Figure 4. The measurements are taken with a Faro Laser Tracker ION having a distance accuracy of 8 μm + 0.4 μm/m, and angular accuracy of 10 μm + 2.5 μm/m. The emitted laser is reflected by an SMR, which is magnetically attached to a *nest*. In our experiment, the target measurement is a 1.5 inch SMR mounted on the tool part (Fig. 4). The measured positions are expressed w.r.t. the laser reference frame ($\boldsymbol{\Phi}_L$) and transformed w.r.t. $\boldsymbol{\Phi}_W$.

We note that the measurement accuracy might be influenced by many aspects, such as environment, duration of operation, and the distance between the target and the laser tracker. Therefore, we evaluated the laser tracker accuracy for our own setup. A calibrated bar with a known length was measured ten times, and the distance error was found to be 26 μm ± 14 μm with 95.4% confidence interval of uncertainty. However, the measurement uncertainty was reduced by taking several measurements at each position.

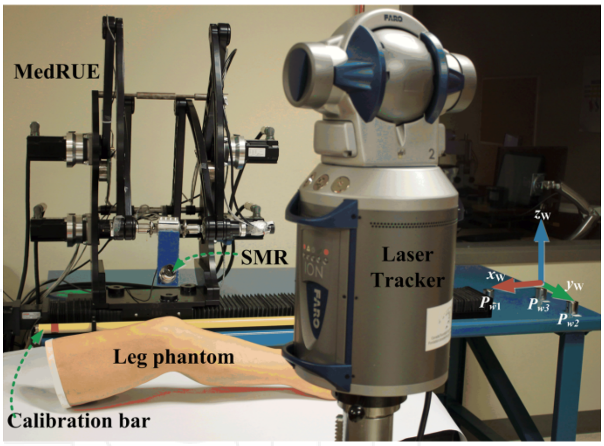

Figure 4. Experiment setup of MedRUE positioning performance assessment and calibration

The results for the position repeatability at the nine measurement points are shown in Table 1. The first row shows the composed repeatability defined in Eq. (21), and the other three rows list the repeatability according to the x, y and z axes. Naturally, the position repeatability at P_1 is worse, which is mainly because the arrivals at P_1 are from eight different directions. Furthermore, the position repeatability along x at P_1 is poorer than along y and z. This is caused by the fact that the motion along the x axis is dominated by the linear guide, which has a backlash of 76 μm according to its manufacturer.

	P_1	P_2	P_3	P_4	P_5	P_6	P_7	P_8	P_9
RP	143	141	54	60	105	99	84	77	50
RP_x	139	136	43	47	96	88	71	61	38
RP_y	74	43	39	43	48	51	52	49	39
RP_z	54	19	18	21	33	28	24	27	18

Table 1. Position repeatability (in μm)

	P_1	P_2	P_3	P_4	P_5	P_6	P_7	P_8	P_9
APA	4.264	1.271	3.849	5.770	0.885	3.788	2.183	2.155	4.792
APA_x	2.217	0.432	1.386	1.823	0.103	1.463	0.568	0.118	2.022
APA_y	1.127	0.129	1.586	2.978	0.677	0.157	1.877	2.124	0.192
APA_z	3.463	1.188	3.222	4.594	0.560	3.491	0.960	0.346	4.340
RPA	—	1.822	1.665	3.018	1.656	2.068	2.058	2.042	1.829
RPA_x	—	0.617	0.886	0.377	0.886	1.074	0.427	0.977	0.569
RPA_y	—	0.340	0.445	2.273	0.460	0.871	0.565	0.896	0.506
RPA_z	—	1.680	1.337	1.950	1.321	1.538	1.932	1.554	1.663

Table 2. Absolute position accuracy (*APA*) and relative position accuracy (*RPA*) before calibration (in mm)

The results for the repeatability at P_1 in the two measurement planes (i.e., planes $C_1C_2C_7C_8$ and $C_3C_4C_5C_6$) are illustrated in Figure 5. On each plane, there are four groups (G_1, G_2, G_3, G_4) of data in different colors indicating four different directions to reach P_1. The measured data are illustrated with an asterisk marker, while the barycentre of each group is a solid circle. The cluster groups are clearly separated from each other. The divergence of measurement on P_1 shows the imperfection of the multidirectional movement caused mainly by the backlash of the mechanical parts of our robot.

The position absolute accuracy and relative accuracy before calibration is given in Table 2. As an early prototype, the robot's poor accuracy is mainly due to its manufacture and assembling errors. The worst case of the absolute accuracy before calibration is about 6 mm, while the worst relative accuracy before calibration is about 3 mm.

4. Kinematic Calibration Experiment

In this section the proposed calibration approach is explained. The actual values of the robot parameters are identified to improve robot accuracy.

Group	Description	Parameters
(1)	The world reference frame	$x_W, y_W, z_W, \gamma_W, \beta_W, \alpha_W$
(2)	Active joint offset error	$\tilde{q}_2, \tilde{q}_3, \tilde{q}_4, \tilde{q}_5$
(3)	Assembling of five-bar mechanisms	$y_{O1}, z_{O1}, y_{O2}, z_{O2}, \theta_1, \theta_2$
(4)	Link lengths of five-bar mechanisms	$l_{10}, l_{11}, l_{12}, l_{13}, l_{14}$, $l_{20}, l_{21}, l_{22}, l_{23}, l_{24}$

Table 3. Kinematic parameters

The parameters expected to be identified are summarized in four groups, as shown in Table 3. Parameters in Group 1 define $\mathbf{\Phi}_W$ in Eq. (30). Group 2 represents the offset of active joints at the home position. Group 3 is named *assembling parameters*, which specifies how the two five-bar mechanisms are assembled on the robot base, by illustrating the position and angle of link L_{i0} on the robot base (Figure 2(a)). Group 4 englobes the lengths of the links of the two five-bar mechanisms.

4.1 The world reference frame parameters

The world reference frame $\mathbf{\Phi}_W$ is defined in the robot's workspace by three SMR nests P_{W1}, P_{W2} and P_{W3} as shown in Figure 4. Assuming P_{W3} is the origin of $\mathbf{\Phi}_W$ and P_{W1} is a point on the x_W axis, then the three unit vectors of $\mathbf{\Phi}_W$ are defined w.r.t. the $\mathbf{\Phi}_L$. The unit vector $\mathbf{x}_W$ is determined by the normalized vector $\frac{\mathbf{p}_{W_{31}}}{\|\mathbf{p}_{W_{31}}\|}$, where $\mathbf{p}_{W31}$ is a vector from P_{W3} to P_{W1} in $\mathbf{\Phi}_L$. The z_W axis of $\mathbf{\Phi}_W$ is defined as the normal of the plane defined by P_{W1}, P_{W2} and P_{W3}. The rotation matrix of $\mathbf{\Phi}_W$ w.r.t. $\mathbf{\Phi}_L$ is written as:

$$ {}^{L}_{W}\mathbf{R} = \left[\mathbf{x}_W, \mathbf{y}_W, \mathbf{z}_W\right]. \tag{25}$$

The transformation matrix of $\mathbf{\Phi}_W$ w.r.t. $\mathbf{\Phi}_L$ is defined as follows:

$$ {}^{L}_{W}\mathbf{T} = \begin{bmatrix} {}^{L}_{W}\mathbf{R} & \mathbf{o}_W \\ \mathbf{0} & 1 \end{bmatrix}, \tag{26}$$

where vector $\mathbf{o}_W$ is the composed by the coordinates of P_{W3}. All measured position data can be represented w.r.t. $\mathbf{\Phi}_W$ by using the transformation matrix ${}^{L}_{W}\mathbf{T}$. A point ${}^{W}\mathbf{P}$ is derived from the laser measured data ${}^{L}\mathbf{P}$ by the following equation:

$$ \begin{bmatrix} {}^{W}\mathbf{p} \\ 1 \end{bmatrix} = {}^{L}_{W}\mathbf{T}^{-1} \begin{bmatrix} {}^{L}\mathbf{p} \\ 1 \end{bmatrix}. \tag{27}$$

For convenience, all the further measured positions, in this paper, are implicitly expressed w.r.t. $\mathbf{\Phi}_W$.

Frame $\mathbf{\Phi}_0$ is defined on the robot base plate, as shown in Figure 1. The top surface of the plate is considered as the x_0y_0 plane. By placing the SMR in n positions on the x_0y_0 plane, a reference plane is fitted from the laser tracker measurement data ($3\times n$ matrix $\mathbf{P}_n = [\mathbf{p}_1,..., \mathbf{p}_n]$, where vector $\mathbf{p}_n$ is the n^{th} measurement). The barycentre of $\mathbf{P}_n$ is $\bar{\mathbf{p}} = \frac{1}{n}\sum_{k=1}^{n}\mathbf{p}_k$. For the smallest eigenvalue of $\bar{\mathbf{P}}_n^T\bar{\mathbf{P}}_n$ (where $\bar{\mathbf{P}}_n = [\mathbf{p}_1 - \bar{\mathbf{p}}, \mathbf{p}_2 - \bar{\mathbf{p}}, \cdots, \mathbf{p}_n - \bar{\mathbf{p}}]$), its corresponding eigenvector approximates the normal vector $\mathbf{z}_0$ of the fitted plane x_0y_0. Finally, the x_0y_0 plane is determined by a point $\bar{\mathbf{p}}$ and the normal vector $\mathbf{z}_0$. The x_0 axis is aligned with the direction of the linear guide and is estimated by measuring an SMR on the robot base, while actuating the linear guide. The method to fit a line from 3D cluster points is similar to the method to estimate the normal vector $\mathbf{z}_0$, except that the vector $\mathbf{x}_0$ is estimated as the eigenvector with largest eigenvalue. Then, the rotation matrix of $\mathbf{\Phi}_0$ w.r.t. $\mathbf{\Phi}_W$ is found as:

$$ {}^{W}_{0}\mathbf{R} = \left[\mathbf{x}_0, \mathbf{y}_0, \mathbf{z}_0\right]. \tag{28}$$

The origin O_0 of $\mathbf{\Phi}_0$ is located on the robot base plate as shown in Figure 2(a). Its coordinates w.r.t. $\mathbf{\Phi}_W$ are obtained by placing an SMR above the robot base plate. The projection of the SMR on x_0y_0 plane provides the coordinates of O_0 as follows:

$$ \mathbf{o}_0 = \mathbf{o}'_0 - \left(\left(\mathbf{o}'_0 - \bar{\mathbf{p}}\right)\cdot\mathbf{z}_0\right)\mathbf{z}_0, \tag{29}$$

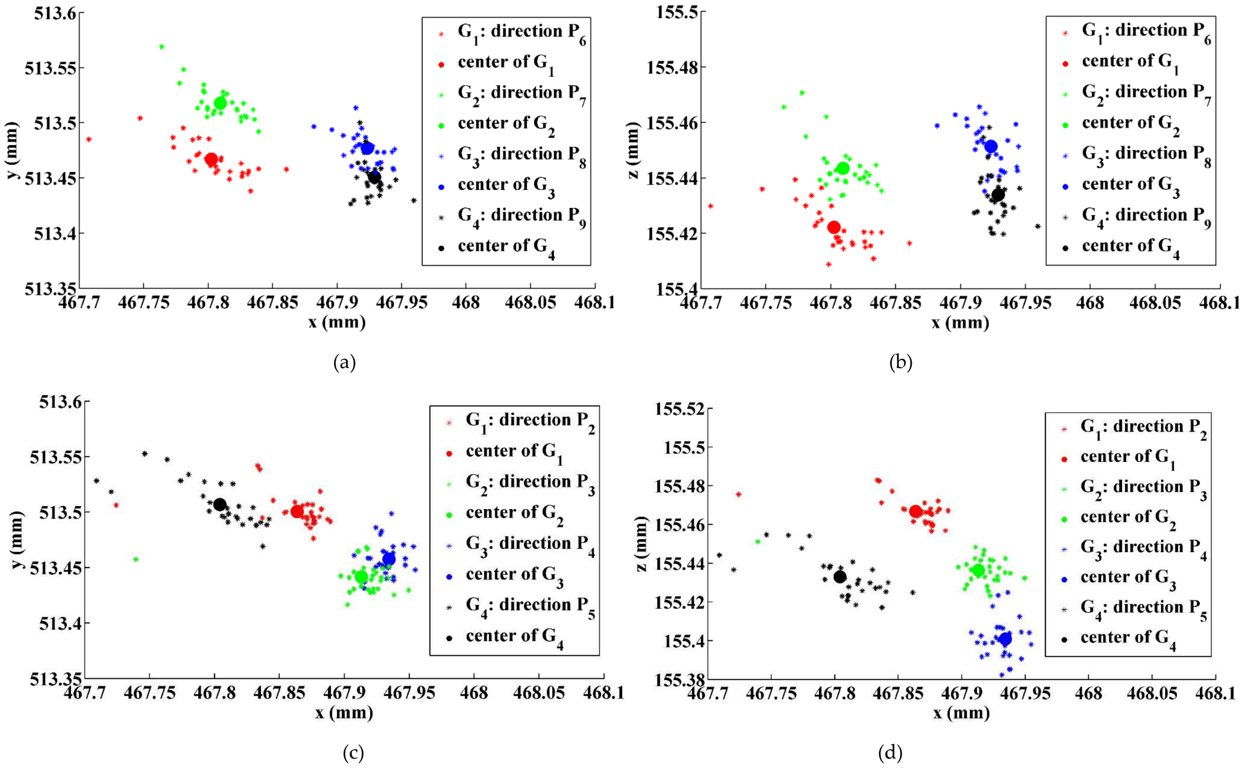

Figure 5. Measurements at P_1, for arrivals from multiple directions: (a) on measurement plane $C_3C_4C_5C_6$, view in xy plane; (b) on measurement plane $C_3C_4C_5C_6$, view in xz plane (c) on measurement plane $C_1C_2C_7C_8$; view in xy plane (d) on measurement plane $C_1C_2C_7C_8$, view in xz plane

where $\mathbf{o}'_0$ is the vector of measured coordinates of the SMR. Then the transformation matrix of $\mathbf{\Phi}_0$ w.r.t. $\mathbf{\Phi}_W$ is obtained as:

$$
{}^{W}_{0}\mathbf{T}(x_W, y_W, z_W, \gamma_W, \beta_W, \alpha_W) = \begin{bmatrix} {}^{W}_{0}\mathbf{R} & \mathbf{o}_0 \\ \mathbf{0} & 1 \end{bmatrix}. \tag{30}
$$

where x_W, y_W, z_W, γ_W, β_W and α_W are the $\mathbf{\Phi}_W$ parameters to be identified: x_W, y_W, z_W are the coordinates of $\mathbf{o}_0$, and Euler angles γ_W, β_W, α_W are obtained from the rotation matrix ${}^{W}_{0}\mathbf{R}$.

4.2 Active joint offset errors

The objective of this subsection is to evaluate the difference between the nominal and the real joint offsets. Active joints q_2, q_3, q_4 and q_5 are considered. As mentioned earlier, the five-bar mechanisms are symmetrically assembled, and therefore are calibrated with the same method. For simplicity, only the calibration of the second five-bar mechanism is demonstrated.

As shown in Figure 6, ten nests (N_i, $i = 1,\ldots, 10$) are attached on the five-bar mechanism for measurement purpose. Four nests (N_i, $i = 3, 4, 7, 10$) are used in this experiment, and the remaining nests are used to identify other parameters.

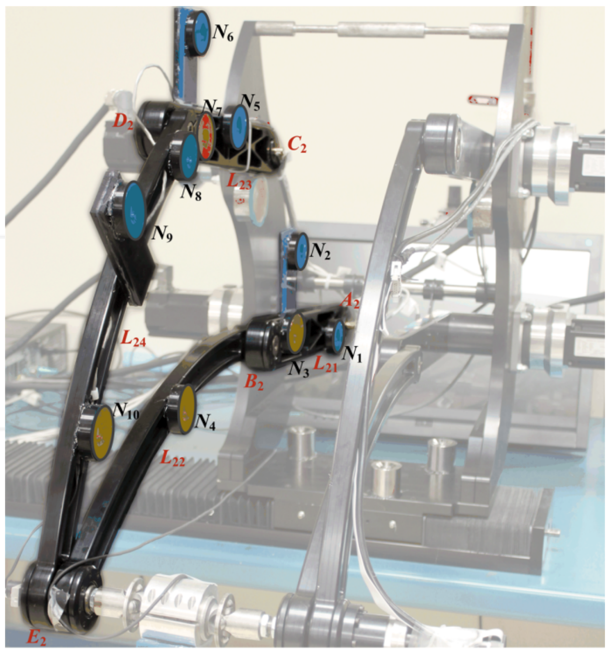

Figure 6. Experiment setup for active joint offset value estimation (nests in orange) and link length estimation (nests in orange and blue) on the second five-bar mechanism

Active joint q_4 directly drives the rotation motion of L_{21}. Thus, the joint offset error of q_4 is assessed via the evaluation of the orientation error of link L_{21} (Figure 2(a)). The orientation of L_{21} is determined by the coordinates of A_2 and B_2. Similarly, the joint offset error of q_5 is assessed via the orientation of link L_{23}, which is determined by the coordinates of C_2 and D_2. Two experiments are designed to obtain the coordinates of A_2, B_2, C_2 and D_2 at the robot home position. The joint offset errors are then evaluated.

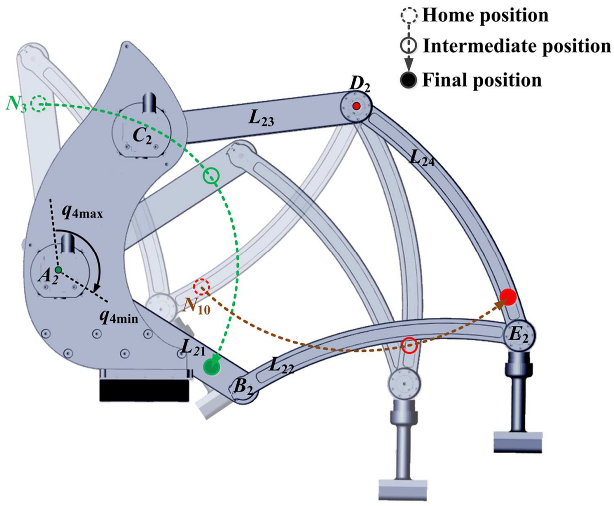

(a)

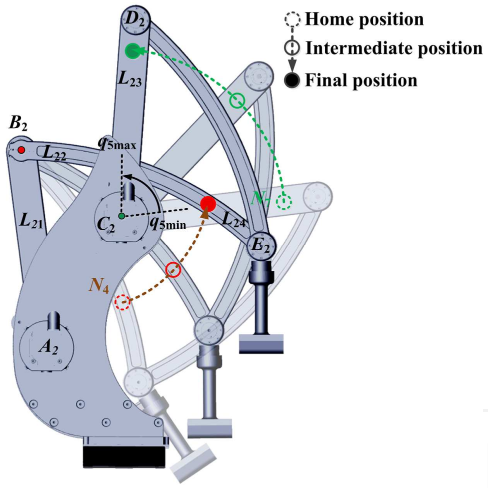

(b)

Figure 7. Path planning in the experiment of active joint offset error (i=1,2): (a) determine coordinates of A_i and D_i, (b) determine coordinates of B_i and C_i.

The first experiment is designed to determine the coordinates of A_2 and D_2 (Figure 7(a)) as follows:

a. Two nests denoted N_3 and N_{10} are attached to links L_{21} and L_{24} respectively, as shown in Figure 6 and Figure 7(a).

b. The robot starts from its home position, which is illustrated with the highest transparent image in Figure 7(a). The angle of joint q_4 is increased gradually with a step of 2°, within a range of 130°. Meanwhile, link L_{23} is kept in its home position throughout the experiment process. At each motion step the robot motion is halted, and measurements of N_3 and N_{10} are taken.

c. The measured positions of N_3 and N_{10} — which follow circular curves centred at A_2 and D_2 respectively — are fitted to two circles [31] in order to determine the coordinate of A_2 and D_2.

For illustration purposes, an intermediate position of MedRUE is illustrated with intermediate transparency, and the opaque image shows the final position of MedRUE. The nests N_3 and N_{10} are demonstrated with a dashed circle, solid circle and filled circle in these positions, respectively.

To determine the coordinates of B_2 and C_2, we used the same approach as for A_2 and D_2. The used nests are denoted N_4 and N_7, and are attached to links L_{22} and L_{23} respectively, as shown in Figure 6. The experiment is illustrated in Figure 7(b).

As shown in Figure 2(a), the coordinates of A_2 and B_2 evaluate the orientation of links L_{21} in the y_0z_0 plane. The orientation of the link L_{21} is driven directly by active joint q_4. Thus, the joint offset $\tilde{q}_4$ is represented by the difference between the nominal value $\hat{q}_4$ and the evaluated orientation of L_{21} at the home position:

$$\tilde{q}_4 = \operatorname{atan2}\left(-\left(y_{B_2} - y_{A_2}\right), \left(z_{B_2} - z_{A_2}\right)\right) - \hat{q}_4, \tag{31}$$

where y_{A2} and z_{A2} are the y and z coordinates of A_2 w.r.t. $\mathbf{\Phi}_0$. Similarly, the joint offset error of q_5 is evaluated by the coordinates of C_2 and D_2.

$$\tilde{q}_5 = \operatorname{atan2}\left(-\left(y_{D_2} - y_{C_2}\right), \left(z_{D_2} - z_{C_2}\right)\right) - \hat{q}_5. \tag{32}$$

The active joint offsets of q_2 and q_3, related to the first five-bar mechanism, are assessed similarly to q_4 and q_5, by using the coordinates of A_1, B_1, C_1 and D_1.

4.3 Assembling parameters

The assembling parameters are y_{O1}, z_{O1}, y_{O2}, z_{O2}, θ_1, θ_2, and these describe the assembly of the two five-bar mechanisms on the robot base. The i^{th} (i = 1, 2) five-bar mechanism is assembled on the robot base at joints A_i and C_i. As shown in Figure 2(a), O_i is the middle point of link L_{i0} defined by A_i and C_i. Angle θ_i illustrates the orientation of link L_{i0} in y_0z_0 plane. Knowing that the coordinates of A_i and C_i are obtained in the previous subsection, the assembling parameters are calculated as follows:

$$y_{M_i} = \frac{y_{A_i} + y_{C_i}}{2}, \tag{33}$$

$$z_{M_i} = \frac{z_{A_i} + z_{C_i}}{2}, \tag{34}$$

$$\theta_i = \operatorname{atan2}\left(-\left(y_{C_i} - y_{A_i}\right), \left(z_{C_i} - z_{A_i}\right)\right). \tag{35}$$

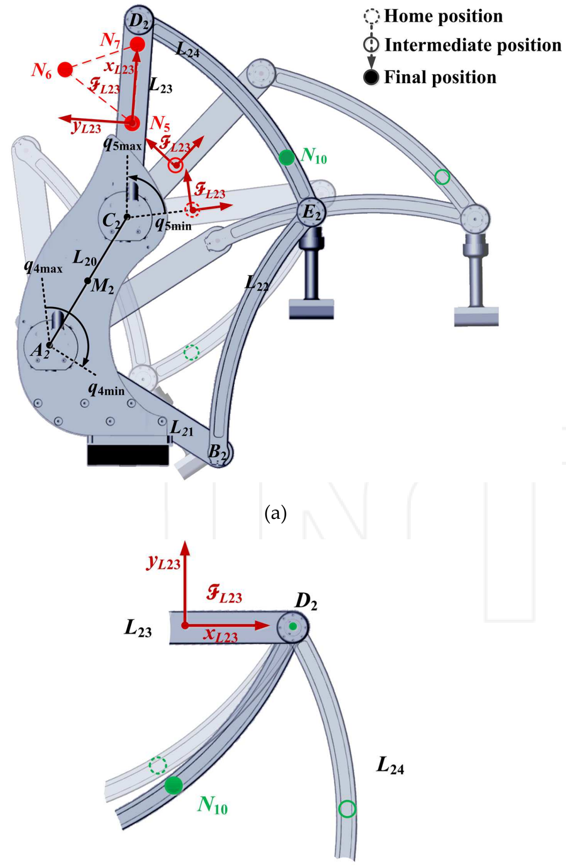

(a)

(b)

Figure 8. Experiment to assess the link length l_{23} (a) link reference frame and nests displacement during robot motion (b) trajectory of nest N_{10} w.r.t. to link reference frame $\mathbf{\Phi}_{L23}$

4.4 Link length parameters

The assessment of the link length parameters is demonstrated using the second five-bar mechanism (i.e., l_{20}, l_{21}, l_{22}, l_{23} and l_{24}), while those for the first mechanism (i.e., l_{10}, l_{11}, l_{12}, l_{13}, l_{14}) are obtained similarly.

The link length of L_{20} is determined by using the coordinates of A_2 and C_2 w.r.t. $\mathbf{\Phi}_0$, which were obtained in subsection 4.2:

$$l_{20} = \sqrt{\left(x_{C_2} - x_{A_2}\right)^2 + \left(y_{C_2} - y_{A_2}\right)^2 + \left(z_{C_2} - z_{A_2}\right)^2}. \tag{36}$$

The identification of l_{21}, l_{22}, l_{23} and l_{24} is carried out by moving simultaneously joints q_5 and q_4 inside their limit ranges, as shown in Figure 8(a).

Note that link L_{20} has both endpoints A_2 and C_2 fixed w.r.t. $\mathbf{\Phi}_0$. However, for the other links, one or both endpoints change position during the experiment. To find the position of endpoints B_2, D_2 and E_2, reference frames are attached to the corresponding links. For example, Figure 8(a) shows a link frame $\mathbf{\Phi}_{L23}$, which is associated with link L_{23} and defined by N_5, N_6 and N_7. Therefore, the movement of the nest N_{10}, seen from $\mathbf{\Phi}_{L23}$ as shown in Figure 8(b), makes a circle centred at D_2. The coordinates of D_2 w.r.t. $\mathbf{\Phi}_{L23}$ are then transformed to be w.r.t. Φ_0.

The coordinates of B_2 and E_2 w.r.t. $\mathbf{\Phi}_0$ are determined in similar ways as D_2. Point B_2 is determined by observing nest N_4 in link reference frame $\mathbf{\Phi}_{L21}$ (built by nests N_1, N_2 and N_3). Then, E_2 is determined by observing nest N_4 in link reference frame $\mathbf{\Phi}_{L24}$ (built by nests N_8, N_9 and N_{10}). With all coordinates of A_2, B_2, C_2, D_2 and E_2 given w.r.t. $\mathbf{\Phi}_0$, the length of the links are estimated as follows:

$$\begin{aligned}
l_{21} &= \sqrt{\left(x_{B_2} - x_{A_2}\right)^2 + \left(y_{B_2} - y_{A_2}\right)^2 + \left(z_{B_2} - z_{A_2}\right)^2} \\
l_{22} &= \sqrt{\left(x_{E_2} - x_{B_2}\right)^2 + \left(y_{E_2} - y_{B_2}\right)^2 + \left(z_{E_2} - z_{B_2}\right)^2} \\
l_{23} &= \sqrt{\left(x_{D_2} - x_{C_2}\right)^2 + \left(y_{D_2} - y_{C_2}\right)^2 + \left(z_{D_2} - z_{C_2}\right)^2} \\
l_{24} &= \sqrt{\left(x_{E_2} - x_{D_2}\right)^2 + \left(y_{E_2} - y_{D_2}\right)^2 + \left(z_{E_2} - z_{D_2}\right)^2}
\end{aligned} \tag{37}$$

4.5 Parameter calibration results and validation

To validate the proposed calibration method, we perform the same experiment with nominal and calibrated parameters. Both the nominal and identified values of calibrated parameters are listed in Table 4.

	Nominal value	**Calibrated value**
Link length of Five-bar mechanisms (unit)		
l_{10} (mm)	150	151.580
l_{11} (mm)	400	400.510
l_{12} (mm)	520	518.605
l_{13} (mm)	400	400.656
l_{14} (mm)	520	523.003
l_{20} (mm)	150	151.007
l_{21} (mm)	400	400.401
l_{22} (mm)	520	523.075
l_{23} (mm)	400	400.926
l_{24} (mm)	520	526.285
Assembling of five-bar mechanisms (unit)		
y_{O1} (mm)	−158	−153.714
z_{O1} (mm)	308	305.442
y_{O2} (mm)	−158	−156.169
z_{O2} (mm)	308	309.001
θ_1 (°)	150	148.906
θ_2 (°)	150	150.583
Active joint offset error (unit)		
$\tilde{q}_2$ (°)	0	1.445
$\tilde{q}_3$ (°)	0	−0.730
$\tilde{q}_4$ (°)	0	1.521
$\tilde{q}_5$ (°)	0	−0.093
The world reference frame (unit)		
x_W (mm)	−110	−115.587
y_W (mm)	−136	−140.868
z_W (mm)	30	27.452
γ_W (°)	0	0.292
β_W (°)	0	−0.057
α_W (°)	0	0.286

Table 4. Nominal and identified parameter values

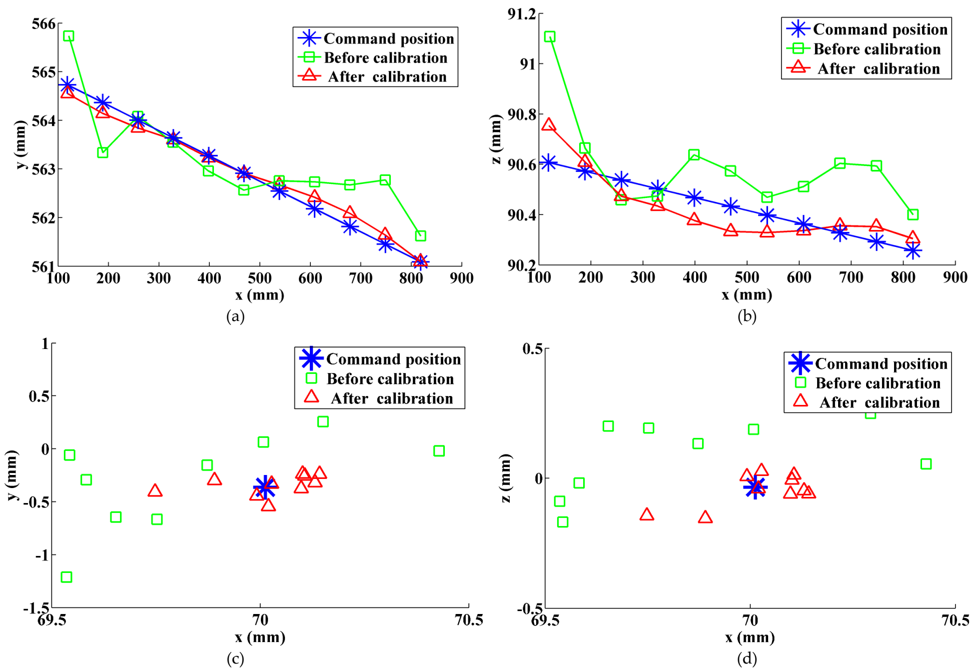

Figure 9. Accuracy improvement in tracking a reference (command) line: Absolute accuracy improvement by observing the trajectory in *xy* plane (a) and *xz* plane (b); Relative accuracy improvement in *xy* plane(c) and *xz* plane (d)

MedRUE is an early prototype of a medical US robot, and there are many imperfections in its manufacture and assembling. As we can see in Table 4, there are noticeable differences between the nominal parameter values and the calibrated parameter values. The majority of errors come from the assembling of the two five-bar mechanisms on the robot base. Furthermore, the manual nest setup (as in Figure 4) for $\mathbf{\Phi}_W$ brings noticeable errors as well. These errors are the main cause of the low accuracy before calibration, as demonstrated in Table 2.

The robot's position accuracy assessment after calibration obtained using the ISO 9283 evaluation approach is shown in Table 5. The maximum absolute position error (i.e., absolute accuracy) has been improved from 5.770 mm before calibration to 0.764 mm after calibration. The relative accuracy is also important in medical application, and its accuracy is satisfactory after calibration. The maximum relative position error was improved from 3.018 mm before calibration to 0.489 mm after calibration, as shown in Table 5.

Figure 9 illustrates the improvement of accuracy when the robot is tracking a reference command line, which is marked in a blue solid line. As shown in Figure 9(a) andFigure 9(b), which represent the trajectory projection on planes *xy* and *xz*, respectively, the trajectory before calibration has a significant error (poor absolute accuracy), and it is greatly improved after the calibration.

Figure 9(c) andFigure 9(d) illustrate the relative position offset between adjacent points. Since the reference command line is created by a set of points with constant offsets, the relative position offsets are represented as a fixed point (illustrated by an asterisk). The obtained offsets before calibration are illustrated by green squares: ideally all these squares should coincide with the reference offset (i.e., the blue asterisk mark). However, they scattered around the reference offset because of the robot parameter residuals. The obtained results (offsets) after calibration are illustrated in red triangles and it clearly demonstrates the improvement of the robot relative accuracy: i.e., the obtained relative position offsets converge towards to the reference offset.

	P_1	P_2	P_3	P_4	P_5	P_6	P_7	P_8	P_9
APA	0.612	0.497	0.449	0.351	0.764	0.341	0.343	0.751	0.576
APA_x	0.527	0.469	0.353	0.309	0.752	0.284	0.341	0.730	0.499
APA_y	0.235	0.152	0.228	0.158	0.053	0.122	0.040	0.165	0.284
APA_z	0.202	0.054	0.155	0.047	0.123	0.144	0.003	0.057	0.020
RPA	—	0.259	0.382	0.253	0.276	0.489	0.396	0.294	0.201
RPA_x	—	0.066	0.132	0.156	0.157	0.313	0.249	0.254	0.029
RPA_y	—	0.107	0.029	0.058	0.212	0.103	0.235	0.070	0.076
RPA_z	—	0.227	0.357	0.191	0.082	0.361	0.198	0.130	0.184

Table 5. Absolute position accuracy (*APA*) and relative position accuracy (*RPA*) after calibration (mm)

The calibration method demonstrated in this section can be used for many other kinds of serial or parallel robots as well. As it is based on direct measurements, it provides more accurate parameter identification than conventional standard calibration methods based on optimization (e.g., forward calibration and reverse calibration method). The proposed method also requires no complex computation (e.g., identification Jacobian matrix, observability analysis) or advanced optimization knowledge in calibration. The comparison between proposed calibration method and standard calibration method are summarized in Table 6.

	Proposed method	Standard calibration method
Kinematic parameter identification	Individually, more accurate	All parameters identified simultaneously, less accurate
End-effector accuracy	Good	Optimized for end-effector accuracy
Complex computation	No	Yes
Robotic calibration knowledge	Basic	Advanced
Time consumption	More time for experiment	Less time for experiment, more time in method developing and computation

Table 6. Comparison of proposed calibration method and standard calibration method

5. Conclusion

An assessment method of the repeatability and the accuracy of a new medical robot were presented. The complete kinematic model of the robot was introduced, and the corresponding parameters were calibrated by a direct measurement method. The proposed method is very easy to implement and requires minimum knowledge of advanced calibration techniques. This approach was validated through experiments which demonstrated a significant improvement of the position accuracy from about 6 mm before calibration to less than 1 mm after calibration. Thus, the presented method has great potential value in robot calibration when advance techniques are not available or not necessary.

6. Acknowledgements

The authors thank the *Canada Foundation for Innovation* and *the Fonds de recherche du Québec sur la nature et les technologies*, who provided the funding for this project.

7. References

[1] Evans, K., Roll, S., and Baker, J. (2009) Work-related musculoskeletal disorders (WRMSD) among registered diagnostic medical sonographers and vascular technologists: a representative sample. Journal of Diagnostic Medical Sonography. 25(6), pp: 287-299.

[2] Gourdon, A., Poignet, P., Poisson, G., Vieyres, P., and Marche, P. (1999) A new robotic mechanism for medical application. Proc. IEEE/ASME International Conference on Advanced Intelligent Mechatronics. 2009 Sep. 19-23. Atlanta, USA. IEEE. pp: 33-38.

[3] Delgorge, C., Courrèges, F., Bassit, L. A., Novales, C., Rosenberger, C., Smith-Guerin, N., Brù, C., Gilabert, R., Vannoni, M., Poisson, G., and Vieyres, P. (2005) A tele-operated mobile ultrasound scanner using a light-weight robot. IEEE Transactions on Information Technology in Biomedicine. 9(1), pp: 50-58.

[4] Pierrot, F., Dombre, E., Dégoulange, E., Urbain, L., Caron, P., Gariépy, J., and Mégnien, J.-L. (1999) Hippocrate: a safe robot arm for medical applications with force feedback. Medical Image Analysis. 3(3), pp: 285-300.

[5] Nelson, T. R., Tran, A., Fakourfar, H., and Nebeker, J. (2012) Positional calibration of an ultrasound image-guided robotic breast biopsy system. Journal of Ultrasound in Medicine. 31(3), pp: 351-359.

[6] Conti, F., Park, J., and Khatib, O. (2014) Interface Design and Control Strategies for a Robot Assisted Ultrasonic Examination System. In: Khatib, O. Kumar, V. and Sukhatme G. Experimental Robotics. Springer Berlin Heidelberg. pp: 97-113.

[7] Koizumi, N., Warisawa, S. i., Hashizume, H., and Mitsuishi, M. (2008) Continuous path controller for the remote ultrasound diagnostic system. IEEE/ASME Transactions on Mechatronics. 13(2), pp: 206-218.

[8] Salcudean, S. E., Zhu, W. H., Abolmasesumi, P., Bachmann, S., and D. Lawrence, P. (1999) A robot system for medical ultrasound. Robotics research International Symposium. Snowbird. 1999 Oct. 9-12. Utah, USA. pp: 195-202.

[9] Abolmasesumi, P., Salcudean, S. E., Zhu, W. H., Sirouspour, M. R., and DiMaio, S. P. (2002). Image-guided control of a robot for medical ultrasound. IEEE Transactions on Robotics and Automation. 18(1), pp: 11-23.

[10] Onogi, S., Urayama, Y., Irisawa, S., and Masuda, K. (2013) Robotic ultrasound probe handling auxiliary by active compliance control. Advanced Robotics. 27(7), pp: 503-512.

[11] Vilchis, A., Troccaz, J., Cinquin, P., Masuda, K., and Pellissier, F., 2003). A new robot architecture for tele-echography. IEEE Transactions on Robotics and Automation, 19(5), pp: 922-926.

[12] Masuda, K., Kimura, E., Tateishi, N., and Ishhara, K. (2001) Three dimensional motion mechanism of ultrasound probe and its application for tele-echography system. Proc. IEEE/RSJ International Conference on Intelligent Robots and Systems. 2001 Oct. 29 -2001 Nov. 03. Maui, Hawaii, USA. IEEE. pp: 1112-1116.

[13] Masuda, K., Kimura, E., Tateishi, N., and Ishihara, K. (2001) Construction of 3D Movable Echographic Diagnosis Robot and Remote Diagnosis via Fast

Digital Network. Proc. 23rd Annual International Conference of the IEEE Engineering in Medicine and Biology Society. 2001 Oct. 25. Istanbul, Turkey. IEEE. pp: 3634-3637.

[14] Nakadate, R., Solis, J., Takanishi, A., Sugawara, M., Niki, K., and Minagawa, E. (2010) Development of the Ultrasound Probe Holding Robot WTA-1RII and an Automated Scanning Algorithm based on Ultrasound Image Feedback. ROMANSY 18 Robot Design. In: Castelli, V. P. and Schiehlen, W. Dynamics and Control. Springer Vienna. pp: 359-366.

[15] Lessard, S., Bigras, P., and Bonev, I. A. (2007) A New Medical Parallel Robot and Its Static Balancing Optimization. Journal of Medical Devices. 1(4), pp: 272-278.

[16] Zhao, L., Yen, A. K. W., Coulombe, J., Bigras, P., and Bonev, I. A. (2013) Kinematic analyses of a new medical robot for 3D vascular ultrasound examination. Transactions of the Canadian Society for Mechanical Engineering. 38(2), pp: 227-239.

[17] Mercier, L., Langø, T., Lindseth, F., and Collins, L. D. (2005) A review of calibration techniques for freehand 3-D ultrasound systems. Ultrasound in Medicine & Biology. 31(2), pp: 143-165.

[18] Lindseth, F., Tangen, G. A., Langø, T., and Bang, J. (2003) Probe calibration for freehand 3-D ultrasound. Ultrasound in Medicine & Biology. 29(11), pp: 1607-1623.

[19] Mooring, B. W., Driels, M. R., and Roth, Z. S. (1991) Fundamentals of Manipulator Calibration. John Wiley & Sons, NY. 329.

[20] Lee, B.-J. (2013) Geometrical Derivation of Differential Kinematics to Calibrate Model Parameters of Flexible Manipulator. International Journal of Advanced Robotic Systems. 10(106).

[21] Joubair, A., Slamani, M., and Bonev, I. A. (2012) Kinematic calibration of a 3-DOF planar parallel robot. Industrial Robot: An International Journal. 39(4), pp: 392-400.

[22] Joubair, A., and Bonev, I. A. (2013) Comparison of the efficiency of five observability indices for robot calibration. Mechanism and Machine Theory. 70, pp: 254-265.

[23] Zhuang, H., Yan, J., and Masory, O. (1998) Calibration of stewart platforms and other parallel manipulators by minimizing inverse kinematic residuals. Journal of Robotic Systems. 15(7), pp: 395-405.

[24] Li, C., Wang, T., Hu, L., Zhang, L., Du, H., Wang, L., Luan, S., and Tang, P. (2014) Accuracy Analysis of a Robot System for Closed Diaphyseal Fracture Reduction. International Journal of Advanced Robotic Systems. 11(169).

[25] Maurine, P., and Dombre, E. (1996) A calibration procedure for the parallel robot Delta 4. IEEE International Conference on Robotics and Automation. 1996 Apr. 22-28. Minneapolis, MN. IEEE. pp: 975-980.

[26] Joubair, A., Zhao, L.-F., Bigras, P., Bonev, I. A., and Loughlin, C. (2015) Absolute accuracy analysis and improvement of a hybrid 6-DOF medical robot. Industrial Robot: An International Journal. 42(1), pp: 44-53.

[27] Barati, M., Khoogar, A., and Nasirian, M. (2011) Estimation and calibration of robot link parameters with intelligent techniques. Iranian Journal of Electrical and Electronic Engineering. 7(4), pp: 225-234.

[28] Renders, J. M., Rossignol, E., Becquet, M., and Hanus, R. (1991) Kinematic calibration and geometrical parameter identification for robots. Robotics and Automation, IEEE Transactions on. 7(6), pp: 721-732.

[29] ISO-9283. (1998) Manipulating industrial robots -- Performance criteria and related test methods. International Organization for Standardization. Geneva, Switzerland.

[30] Joubair, A., Slamani, M., and Bonev, I. A. (2012) A novel XY-Theta precision table and a geometric procedure for its kinematic calibration. Robotics and Computer-Integrated Manufacturing. 28(1), pp: 57-65.

[31] Taubin, G. (1991) Estimation of planar curves, surfaces, and nonplanar space curves defined by implicit equations with applications to edge and range image segmentation. IEEE Transactions on Pattern Analysis and Machine Intelligence. 13(11), pp: 1115-1138.